

Stress related magnetic imaging of iron-based metallic glass produced with laser beam powder bed fusion

Julia Löfstrand^{a,1}, Inga K. Goetz^{a,1}, Jithin J. Marattukalam^a, Björgvin Hjörvarsson^a, Gyula Nagy^a, Björn Skårman^b, Martin Sahlberg^c, Petra E. Jönsson^{a,*}

^a Department of Physics and Astronomy, Materials Physics, Uppsala University, Box 516, Uppsala, SE-75120, Sweden

^b Höganäs AB, Höganäs, SE-26383, Sweden

^c Department of Chemistry, Inorganic Chemistry, Uppsala University, Box 523, Uppsala, SE-75120, Sweden

ARTICLE INFO

Keywords:

Bulk metallic glass (BMG)
Laser beam powder bed fusion (PBF-LB/M)
Selective laser melting (SLM)
Kerr microscopy
Thermal stress

ABSTRACT

Additive manufacturing makes the production of bulk metallic glasses possible in thicknesses exceeding the critical casting thickness. However, a crucial challenge is the build-up of thermally induced stress, often resulting in printed parts suffering from cracking. In this study, the process parameters are optimised for printing soft-magnetic metallic glass samples of an Fe-based alloy ($\text{Fe}_{73.8}\text{P}_{10.6}\text{Mo}_{4.2}\text{B}_{2.3}\text{Si}_{2.3}\text{C}_{6.7}$), using laser beam powder bed fusion. In addition, the structural and magnetic properties of as-received and heat-treated powder are investigated and compared to those of the printed samples. Kerr microscopy is used for imaging the magnetic domains on single track cross-sections produced on top of a polished printed sample. This reveals the shape of the melt pool of a single laser track, as well as the magnetic domains around it and in other regions of the printed sample. The shape and size of the magnetic domains reflect the residual stress in the sample through the effect of magneto-elastic coupling. This magnetic contrast could be used to get further insights into how to control the development of stress during the printing process.

1. Introduction

Additive manufacturing (AM) techniques such as laser beam powder bed fusion (PBF-LB/M) have proven useful for the production of functional materials that are brittle or require high cooling rates to reach their ideal state [1–4]. An important class of functional materials requiring high cooling rates are the metallic glasses. They exhibit unique mechanical properties [5–7], high corrosion resistance [8], catalytic properties [9], and excellent soft-magnetic properties [10]. Metallic glasses have traditionally been synthesised using different rapid solidification techniques, such as melt spinning and suction casting, with cooling rates of typically 10^5 – 10^6 K/s [11]. With these techniques, bulk metallic glasses (BMGs) with high glass-forming ability can be produced in thicknesses up to typically a few millimetres [10]. This critical casting thickness can be exceeded in PBF-LB/M additive manufacturing, since the sample is built linewise, layer by layer, with rapid local heating and cooling as the laser is scanned across the build [12–14]. PBF-LB/M additive manufacturing is therefore one of the most promising techniques for

producing parts of metallic glass alloys of almost arbitrary shape [15]. An additional advantage of this technique is the possibility to locally control the microstructure [16].

Using soft-magnetic materials with low losses in inductive applications is of great importance for increasing the efficiency of the entire electrical energy system [17,18]. As an example, in 2008 the sum of all world-wide annual transformer core losses was estimated to be 285 TWh and it was estimated that these losses could be cut in half if the soft-magnetic transformer core material was changed from the most commonly used Si-steel to commercially available soft-magnetic metallic glass alloys [19]. While applications for soft-magnetic metallic glasses with simple geometries are commercially available (such as transformer cores made out of thin metallic glass ribbons), the soft-magnetic parts in electrical machines can have highly complicated shapes. Effective fabrication methods for such metallic glass cores have yet to be developed [20]. The option to additively construct soft-magnetic metallic glass parts with complex shapes is therefore very attractive, in particular since it opens up for opportunities to create entirely new machine

* Corresponding author.

E-mail address: petra.jonsson@physics.uu.se (P.E. Jönsson).

¹ Shared first authorship.

designs [21–24]. However, AM comes with its own set of complications [25]. Much effort is required when optimising the printing methodology as well as the process parameters. Otherwise, the components can be prone to cracking, have high porosity, or not the sought-after structure [26–28,9,29,30]. Structural changes during PBF-LB/M printing of metallic glasses, such as nanocrystallisation, most often occur in the heat affected zone (HAZ) [31,32], where the reheating temperature is above the crystallisation temperature for a short time during the printing process [13]. Depending on which crystalline phase forms, as well as the size of the nanocrystallites, this can either enhance or deteriorate the soft-magnetic properties [11]. It has been shown that for AM of metallic glasses, a low crystal growth rate is more important than a high glass forming ability when the intention is to avoid nanocrystallites in the HAZ [33]. With this in mind, there is still room for improvement in regard to tailoring the alloy compositions. However, it is not the only way to control and improve the material and often the best glass-former does not give the best soft-magnetic performance. Therefore, the key to unlocking the full potential of PBF-LB/M printing of soft-magnetic metallic glasses lies, to a large extent, in the processing.

Adjusting the printing process to reduce residual stress is still one of the major unsolved challenges for AM of metals [34,35]. High local stress might result in cracking, especially for brittle metallic glasses requiring rather high thermal gradients to achieve the amorphous state. The printing methodology has a large influence on the thermal stress. For instance, it has been shown that a chessboard printing pattern as well as low-energy laser re-scanning are useful processing options for minimising the cracking of metallic glasses [26,29,36]. The ability to visualise the stress profile would be a great advantage when optimising the printing methodology and parameters. Traditional non-invasive stress- and microstructural analysis methods based on diffraction are not easily applied on amorphous materials due to their homogeneity and lack of long range order. However, residual stress also affects the magnetic properties through the magneto-elastic coupling [37,38] and causes stress-induced magnetic anisotropy, which can be used to our advantage. The anisotropy energy associated with magneto-elastic coupling can be described as:

$$E_{\sigma} = -K_{\sigma} \cos^2(\theta) = -\frac{3}{2} \sigma \lambda \cos^2(\theta) \quad (1)$$

where σ is the strain, θ is the angle between the magnetisation and the local strain, and λ is the magnetostriction constant. If λ is positive, as for amorphous Fe-based metallic glasses [11], the local anisotropy easy axis is parallel to the local residual stress. Hence, by probing the outcome of the magnetoelastic effects, it is possible to obtain information about the local stress, using methods such as Kerr microscopy [39], which is one of the main tools employed in this study. This technique is based on the magneto-optic Kerr effect (MOKE), i.e. that polarised light that is reflected off of a magnetic surface will shift its polarisation in a manner which is linearly dependent on the local magnetisation [40]. With this method, it is possible to image magnetic domains and see in real-time how they are affected by an applied magnetic field.

In the present study, we investigate thermal, structural, and magnetic properties as well as residual stress in a metallic glass with the composition $\text{Fe}_{73.8}\text{P}_{10.6}\text{Mo}_{4.2}\text{B}_{2.3}\text{Si}_{2.3}\text{C}_{6.7}$ (at.%). The properties of as-received and heat-treated powder are compared to samples printed by PBF-LB/M. Utilising the relation between stress and magnetic anisotropy, the direction of the residual stress is deduced from Kerr microscopy images. In addition, we demonstrate the possibility to image the shape and size of the PBF-LB/M melt pool using Kerr microscopy and a single track approach to isolate the melt pool characteristics from the complex overlapping printing patterns that compose the PBF-LB/M build. The origin of the domain pattern inside the melt pool, captured by the MOKE contrast, is the compressive stress caused by the thermal compression during cooling. The larger surrounding domains and their radial direction around the melt pool are influenced by the tensile stress in the surrounding parts. We conclude that MOKE imaging is an excellent tool to visualise the local residual stress together with defects, such

as cracks and pores, in printed parts of soft-magnetic metallic glasses. The detailed knowledge gained from magnetic metallic glasses concerning the influence of the printing parameters on stress in the build can additionally be useful for understanding the PBF-LB/M process as a whole.

2. Materials and methods

All herein presented samples are based on gas-atomised powder with the composition $\text{Fe}_{73.8}\text{P}_{10.6}\text{Mo}_{4.2}\text{B}_{2.3}\text{Si}_{2.3}\text{C}_{6.7}$ (at.%) supplied by Höganäs AB. The presented composition was determined by inductively coupled plasma - optical emission spectrometry (ICP-OES), and the contents of lighter elements including C, O, N, and S were analysed using the LECO combustion method. The density of $7.22(3) \text{ g/cm}^3$ was measured using a pycnometer. The imaging of the morphology of the powder as well as the cross-section profile of a printed part was performed using scanning electron microscopy (SEM) with a Zeiss LEO 1550. All structural analysis was performed with X-ray diffraction (XRD) using a Bruker D8 Powder system a Lynxeye XE-detector and Cu K- α radiation in Bragg-Brentano geometry. A LakeShore 7404 vibrating sample magnetometer (VSM) was used to measure magnetic hysteresis loops.

Differential scanning calorimetry (DSC) was performed using NETZSCH STA 449C instrument with an oxygen trap system (OTS). The sample was placed in an Al_2O_3 crucible and a continuous heating rate of 20 K/min was applied with argon as the protective gas. Based on the results from the DSC measurement, three temperatures were selected for annealing of the powder, just above the onset of each exothermic reaction. The purpose of using temperatures slightly above the reaction onset was to identify which phases are forming when the sample is heated, as well as the impact of crystallisation on the magnetic properties. Subsequently, three powder samples were enclosed in vacuum ampules and heat treated at 500 °C for two days, at 540 °C for two days, and at 670 °C for one day, followed by water quenching. The heat treated powder samples were then analysed with XRD.

The Fe-based amorphous powder was processed in an EOS M100 (EOS GmbH) in argon atmosphere (purity > 99.9997%) with an overpressure of 30 - 60 mbar compared to ambient conditions. The system is equipped with a Yb-fibre laser having a minimum beam diameter of 40 μm at the focal plane [41]. The samples were built using a chessboard inspired island-based scanning pattern with 67° rotation. The scan speed was set to 1200 mm/s and the layer thickness was 20 μm . The laser power and hatch spacing were varied in the range of 110-170 W and 130-220 μm respectively. The sample area was up to 5×5 mm² and thickness was ≥ 1 mm. The samples were produced in two versions: printed directly on a steel substrate and printed on a support structure so that they could easily be removed from the substrate. The first version was used for Kerr imaging and the second for VSM and XRD analysis.

From the investigated parameter space, four samples (I-IV) were selected for further analysis. Sample I was built with the power 110 W and hatch spacing 140 μm , sample II with 130 W and 140 μm , and sample III and IV with 110 W and 130 μm . For imaging, the additively manufactured samples had to be polished. They were first embedded in bakelite and then polished using a series of steps including diamond suspension to obtain a mirror-like surface. In the last step, SiO_2 -suspension was used to alleviate stress caused by the polishing. The top-surface, i.e. the build plane, was polished for sample I, II and IV. Sample III was instead polished to reveal the cross-section, along one of the sample edges. Sample IV was selected for the single track study, where single laser tracks were produced on the polished top-surface in order to study the effects of processing in closer detail. The single tracks were produced with 110, 130, and 150 W laser power and a laser scan speed of 1200 mm/s. A cross-section was then cut through the single tracks to reveal the plane normal to the scanning direction of the laser. This cross-section was polished, with the same method as previously described. SEM imaging was carried out with a secondary electron (SE) detector to image the surface and a backscattering electron (BSE) detector to investigate Z-contrast.

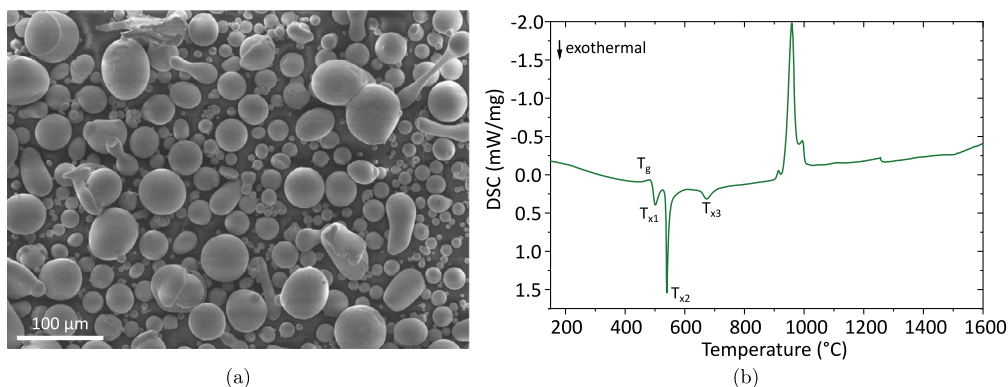


Fig. 1. (a) SEM image of powder particles (b) DSC measurement with a heating rate of 20 K/min. Crystallisation onset temperatures and enthalpies: 486, 528, 649 °C (17, 44, 11 J/g). Melting onset temperatures and enthalpies: 904, 925, 980 °C (-2, -120, -7 J/g).

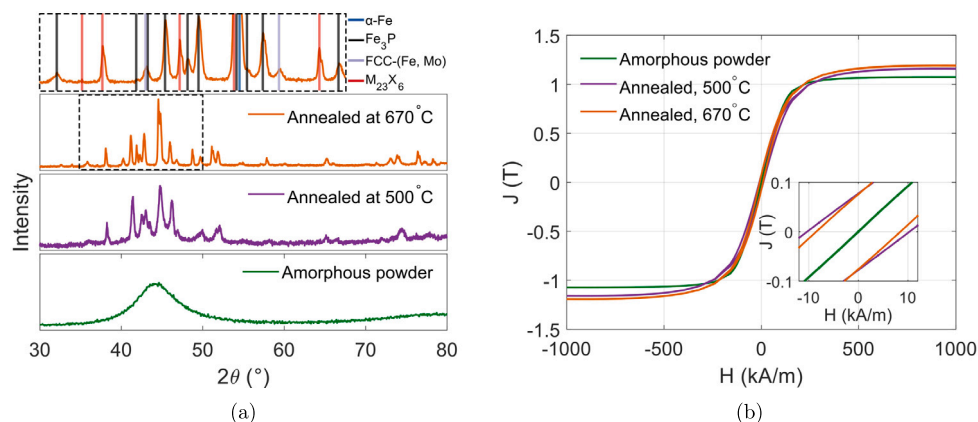


Fig. 2. a) XRD patterns of the as-received powder and powder annealed at 500 and 670 °C, respectively. b) Corresponding magnetic hysteresis loops with an inset showing a close up indicating the coercivities.

The sample was later etched with Aqua Regia for 10 s in an attempt to enhance any crystalline features, but no additional contrast within the printed sample region was achieved.

Compositional mapping was carried out at the scanning nuclear microprobe beamline [42] in the Tandem Laboratory of Uppsala University [43], using micro-elastic backscattering spectrometry (μ -EBS). A He^{2+} beam was focused to a spot of $\sim 5 \mu\text{m}$ and scanned across the single track cross-section. The primary beam energy was set to 3045 keV in order to allow for the detection of oxygen slightly under the surface by the use of the narrow $^{16}\text{O}(\alpha, \alpha_0)^{16}\text{O}$ resonance [44]. The backscattered projectile particles were detected by an annular-type solid-state particle detector. Element maps were constructed by the selection of element specific regions in the EBS spectra for each beam position coordinate on the sample, with the spectrum counts in these regions corresponding to the yield for that element in the corresponding coordinate. Particle-induced X-ray emission (PIXE) spectra were simultaneously captured and μ -PIXE element maps were constructed similarly to those for μ -EBS.

An evico magnetics Kerr microscope was used for magnetic imaging, revealing the magnetic domain structure of the polished surfaces of all selected samples. The Kerr microscope can measure in three different modes: Longitudinal, transversal, and polar. These modes each represent a component of the magnetisation that is detected in relation to the plane of incidence of the light. The top view images were taken in a combination of longitudinal and polar mode, for maximum contrast, however it was the polar (out of plane) component which contributed the most. The single track images were taken in pure versions of each of the three modes. All images shown were taken at the state of magnetic remanence and a differential image is presented, with either a saturated (top view images of sample I and II) or demagnetised (all cross-section images) state used as the background image. The difference in choice of

background image was motivated by a field induced translation of the samples in the cross-section images at saturation, relative to the position they had in remanence. Using the saturated image as the background image would in those cases have introduced artefacts in the differential image from this slight shift in sample position.

3. Results and discussion

3.1. Characterisation of as-received and heat-treated powder

The as-received powder, shown in Fig. 1a, consist of smooth spherical particles with a particle size distribution of 15–45 μm . The thermal characterisation of the as-received powder, depicted in Fig. 1b, shows a clear trace of the glass transition with an apparent onset (T_g) at approximately 470 °C for a heating rate of 20 K/min. No plateau indicating the super-cooled liquid region is observed. Instead, the first crystallisation event directly succeeds the glass transition. There are in total three crystallisation events (T_{x1} , T_{x2} , and T_{x3}), where the largest crystallisation enthalpy with 44 J/g is observed for the second event. The following endothermic melting also occurs in three steps, with the initial onset close to 900 °C. From the observed crystallisation events, the temperatures at exothermic maxima were used in three heat treatments, to identify the structural and magnetic properties of the crystallised material.

Fig. 2a shows the XRD-patterns of the as-received amorphous powder, together with the measurements corresponding to the powders annealed at 500 and 670 °C. The powder annealed at 540 °C has a similar level of crystallinity and the same phases as the one annealed at 670 °C and will therefore not be included in the further discussion. The material databases ICDD and Pearson were used for the phase identification of the powder annealed at 670 °C. The crystallised material is found to

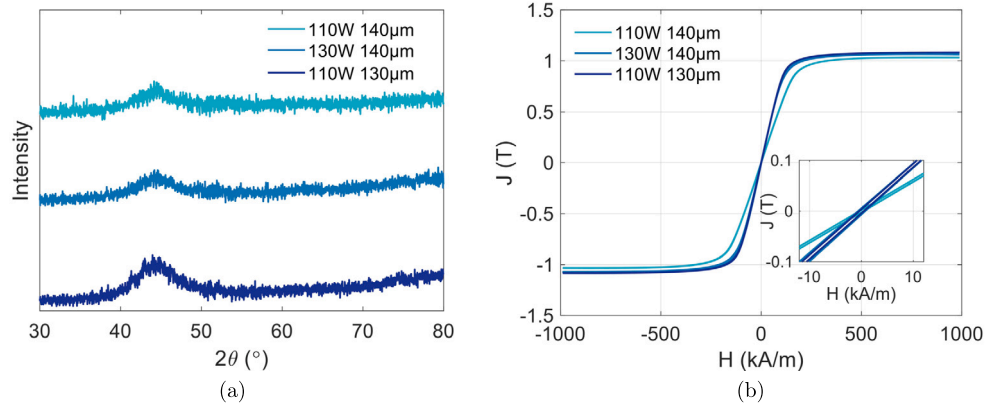


Fig. 3. a) XRD patterns of three printed samples with the parameters 110 W 140 µm, 130 W 140 µm, and 110 W 130 µm b) Corresponding magnetic hysteresis loops measured with VSM. The density was estimated using the measured density of the original powder.

Table 1
Magnetic saturation of the amorphous powder as well as the powders annealed at 500 and 670 °C.

Powder samples	Magnetic saturation, J_s
Amorphous powder	1.07(5) T
Powder annealed at 500 °C	1.16(6) T
Powder annealed at 670 °C	1.19(6) T

Table 2
Magnetic saturation of samples with the three combinations of printing parameters in focus.

Power	Hatch spacing	Magnetic saturation, J_s
110 W	140 µm	1.03(5) T
130 W	140 µm	1.07(5) T
110 W	130 µm	1.08(5) T

consist of phases with structures matching α -Fe ($Im\bar{3}m$) [45], FCC-(Fe, Mo) ($Fm\bar{3}m$) [46], Fe_3P ($I\bar{4}$) [47] and $M_{23}X_6$ ($Im\bar{3}m$) [48].

The VSM measurements of the as-received powder and the powder samples annealed at 500 and 670 °C show the effect of the crystalline fractions on the magnetic properties of the alloy (Fig. 2b). Both the magnetic saturation and coercivity are found to increase with annealing. The measured values of J_s are reported in Table 1. A higher J_s is a reasonable result given the presence of α -Fe with high saturation magnetisation. The increased coercivity is also expected from the presence of the crystallites, which nucleate and grow upon annealing.

3.2. Characterisation of additively manufactured bulk samples

XRD-patterns obtained from three printed samples with the selected printing parameters are shown in Fig. 3a. The diffraction reveals that all samples are X-ray amorphous, to the degree which can be confirmed with the achieved signal-to-noise ratio. Fig. 3b depicts the measured magnetic hysteresis curves of the corresponding samples. Just like the amorphous powder, the samples show soft-magnetic properties with a $H_c < 1$ kA/m, and J_s of ~ 1 T. Within the uncertainty of the measurements, the magnetic saturation does not differ between the samples, as seen in Table 2. The difference in slope is likely caused by the fact that the measured samples were solid pieces of an uneven geometry and thus the demagnetising factor, which is dependent on the shape of the samples, could be slightly different for the different samples. The outcome that it is possible to produce three very similar samples using a range of slightly different parameters shows that there is some tolerance in the production of these materials.

Kerr images of the top view of the polished sample I and II are shown in Fig. 4. The images show the magnetic domains in remanence, with the

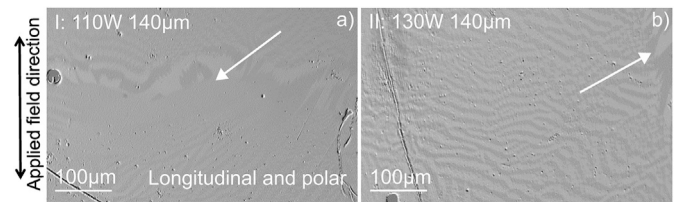


Fig. 4. Kerr images from the polished top-surface of samples a) I and b) II. White arrows indicate areas of larger magnetic domains, while both samples also exhibit regions of maze-like domain patterns. The image was taken with the samples in remanence. The magnetic field used to initially magnetise the samples close to saturation was applied in the sample plane, as indicated.

fully saturated single domain image as the background. The polar signal was found to be the dominating contribution to the contrast, suggesting that the magnetisation is, to a large extent, out of plane. When taking these images, other areas of the samples were also investigated and the domains in both samples have a combination of maze-like domains as well as broader features (pointed out with white arrows in Fig. 4). Some cracks and pores are also evident in these images. Cracking is in itself indicative of the stress built up during the printing process and the presence of pores is a common defect appearing in additively manufactured samples as a consequence of melt pool instability. A benefit of Kerr microscopy, related to this, is the possibility to view the magnetic domains together with these defects. It becomes possible to directly evaluate the influence defects might have regarding e.g. stress relief, as well as the effects of different scanning paths or parameters.

Further information can be gained from the cross-section profile of printed samples, since the magnetic anisotropy is directed mainly in the build direction. The cross-section of a printed piece was investigated for sample III. The Kerr images reveal diverse magnetic landscapes, shown in Fig. 5, with larger domains at the surface, then smaller just below, followed by larger domains further down in the build. This can be related to the complex stress situation in these PBF-LB/M printed samples, which is also a subject of interest for predictive modelling [49–52]. Similar domain behaviour in soft-magnetic BMG ribbons has been observed in previous studies where it was linked to the tensile and compressive stress, yielding large domains in the direction of the stress induced anisotropy in the areas experiencing tensile stress and smaller domains in regions which are in a state of compression [53]. The corresponding areas to these different states of stress are marked out in Fig. 5c.

To isolate the features of the PBF-LB/M melt pool, the top-surface of sample IV was polished and processed with non-overlapping single track laser scans. This way, the base material is still the same, but the single tracks and their corresponding HAZ can be viewed without the influence of other laser tracks created on top or overlapping to the sides. Kerr images of sample IV in cross-section with the single track of the

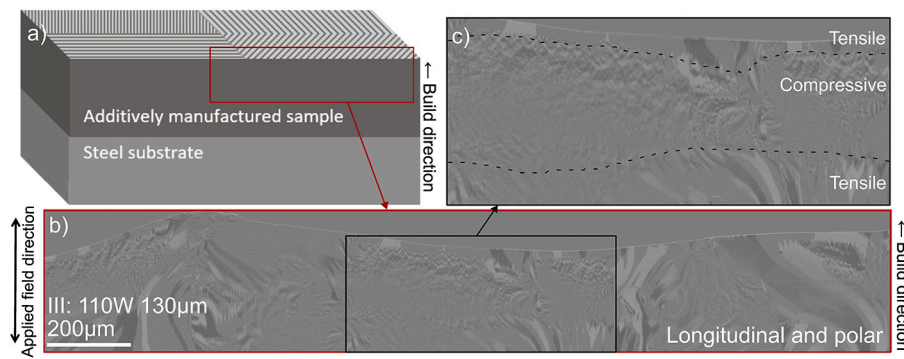


Fig. 5. a) Schematic overview of the printed piece, Sample III, illustrating the investigated region b) Kerr microscopy image overview, taken with a combination of longitudinal and polar signal for maximum contrast c) Close-up with tensile and compressive stress states marked out.

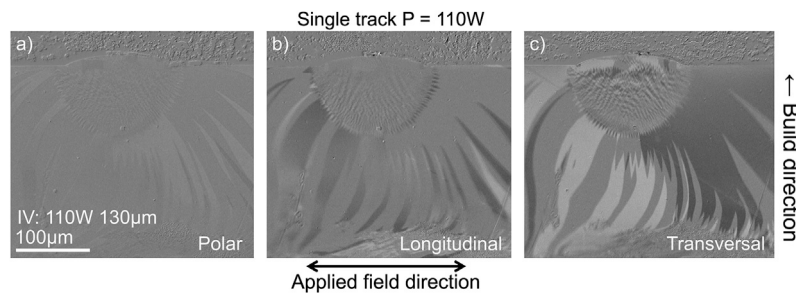


Fig. 6. Single track of 110 W, imaged with Kerr microscopy using a) polar mode b) longitudinal mode and c) transversal mode. The field was applied in the sample plane and perpendicular to the single track.

power 110 W are displayed in Fig. 6. The images show the magnetic domains in remanence for the polar, longitudinal, and transversal mode. The relatively large domains in the areas surrounding the melt pool indicate that the material is magnetically soft and rather homogeneous, with minimal pinning of the domains. The smaller domains in and at the border of the melt pool suggest that there is significant compressive stress within the melt pool, and the direction of the flame-like larger domains surrounding it is a sign of tensile stress in its radial direction. The contrast of the Kerr image in the transversal mode (Fig. 6c) as well as the direction of the domain stripes show clearly that the stress in the area around the melt pool is directed vertically with respect to the build plane and towards the melt pool. This is a reasonable result considering the stress profile originating in the thermal expansion during melting and the following shrinkage compared to the surrounding material [52,54].

Looking at the top of the melt pool, the domains are larger, indicating that they are not under compressive stress, which is reasonable considering that they are free, with no attachment or interface except to the surrounding air or loosely to the bakelite embedding. The same domain behaviour is seen in sample III in Fig. 5. The melt pool of the single track has a conductive mode shape, which is known to be ideal for high density in PBF-LB/M printing. This way of imaging the shape and size of the melt pool can support efforts to tailor the melt pool, which is useful when considering factors such as controlled crystallisation [16]. Between melt pools, shown in Supplementary Figure S.1, the smaller domains are not present in the same extent for sample IV, compared to sample III. This is an expected result, considering that sample IV had a polished top-surface and the images of that sample show the behaviour close to the substrate, unlike sample III where the as-produced surface section is in focus.

Other single tracks produced with 130 W and 150 W were also investigated and Kerr images of these are shown in Supplementary Figure S.2. The single track made with 150 W also appears to have incipient key-hole features [55]. The 150 W track was polished to a position where a pore inside of the melt pool is clearly visible. The presence of this void

has a seemingly less dramatic impact on the domain structure in terms of size and directionality than the melt pool interface.

The areas around and including the single track melt pools on sample IV were additionally studied in cross-section using SEM and the ion based technique μ -EBS. An overview of the main techniques used to study the shape and composition of the single track of 110 W is shown in Fig. 7, with a schematic of the studied sample area in Fig. 7a. The result from SEM imaging using the backscattering electron (BSE) detector is shown in Fig. 7b. There is no contrast which could be related to the melt-pool nor the HAZ, which was also the case for the secondary electron detector. However, in the shown BSE-image, one can distinguish the interface between the steel substrate and the printed BMG. Additional images with higher magnification are included in Supplementary Figure S.3-5. Fig. 7c shows the Fe map as a result of the μ -EBS measurement. Maps were additionally constructed for Mo and O. A summary of these results can be found in Supplementary Figure S.6, which also includes the separate Fe signal with a scaling bar, as well as the Fe signal identified simultaneously with PIXE in Figure S.7. All measurements indicate that the sample composition is homogeneous at the μ -meter scale within the area which exhibits a clear contrast in the Kerr images, as shown for comparison in Fig. 7d.

4. Conclusions

In this work, $\text{Fe}_{73.8}\text{P}_{10.6}\text{Mo}_{4.2}\text{B}_{2.3}\text{Si}_{2.3}\text{C}_{6.7}$ (at.%) bulk metallic glass has been successfully printed using laser beam powder bed fusion and shows no detectable levels of crystallinity, low $H_c < 1$ kA/m, and a relatively high J_s of ~ 1 T. In order to study how the process parameters influence the melt pool characteristics, single tracks were fabricated onto the polished surface of a printed part. No contrast was observed by secondary or backscattered electron imaging. Kerr microscopy was used to achieve an image through the magnetic contrast instead, which showed the magnetic domain structures associated with the melt pool.

We conclude that the shape of the magnetic domains reflects the residual stress via the magneto-elastic coupling, indicating tensile stress around the melt pool and compressive stress within. In addition, this

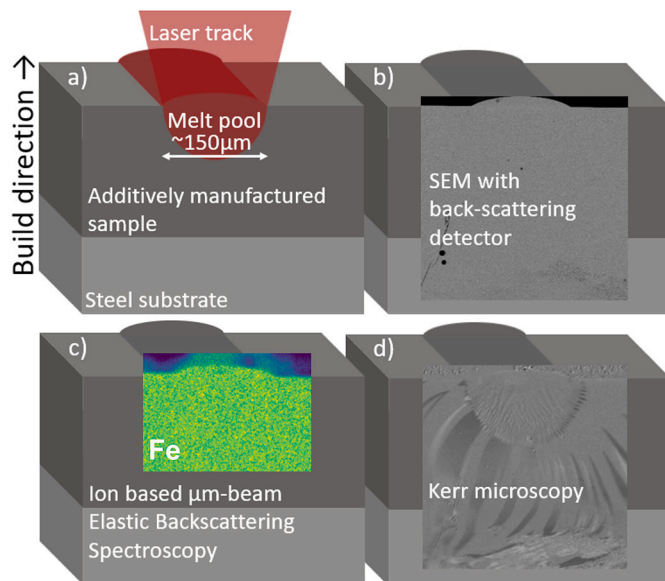


Fig. 7. a) Schematic overview of a single track being produced on top of sample IV, a printed piece with a polished top-surface. b) An SEM image taken with a backscattering detector, showing the cross-section profile of the single track, but no contrast from nanocrystallinity in the heat affected zone. c) EBS image showing the Fe signal which also appears to be homogeneous. d) Single track with magnetic domain contrast measured with Kerr microscopy, showing the shape of the melt pool. The melt pool has small domains inside it and larger domains outside, emanating from the boundary of the melt pool as would be expected from stress originating in the thermal profile of the single track.

gives a clear contrast of the melt pool shape and size, which was not possible with electron microscopy. When it comes to metallic glasses, these features are far more challenging to investigate by traditional diffraction and microscopy techniques compared to crystalline alloys. Consequently, we suggest this Kerr microscopy based approach as an accessible alternative for evaluating both residual stress and melt pool characteristics in additively manufactured magnetic amorphous alloys. It could also be used to relate stress to microstructural features, such as cracks and pores, common for this production method.

In summary, the production parameters, and in extension the physical properties of these materials, can be improved by using magnetic imaging as a tool to view and optimise melt pool size and shape as well as characterising build-up of stress. This methodology shows great promise and has not been used in this combination with laser beam powder bed fusion of bulk metallic glass before. These findings will support further development of the printing parameters of more Fe-based bulk metallic glasses for energy applications and functional components. The knowledge gained from such studies would also be valuable for the printing of non-magnetic metallic glasses.

CRediT authorship contribution statement

Julia Löfstrand: Writing – original draft, Visualization, Project administration, Investigation, Conceptualization. **Inga K. Goetz:** Writing – original draft, Visualization, Investigation, Conceptualization. **Jithin J. Marattukalam:** Investigation. **Björgvin Hjörvarsson:** Supervision, Resources, Funding acquisition. **Gyula Nagy:** Visualization, Investigation, Data curation. **Björn Skårman:** Resources, Investigation. **Martin Sahlberg:** Supervision, Resources. **Petra E. Jönsson:** Writing – review & editing, Supervision, Funding acquisition, Conceptualization.

Declaration of competing interest

The authors declare that they have no known competing financial interests or personal relationships that could have appeared to influence the work reported in this paper.

Data availability

Data will be made available on request.

Acknowledgements

The authors would like to thank Damian Holzapfel for the help with the thermal analysis at RWTH Aachen as well as Henry Stopfel and Gabriella Andersson at Uppsala University for insightful advice regarding Kerr microscopy, and Pedro Berastegui for the SEM imaging of the polished cross-section.

We acknowledge Myfab Uppsala for providing facilities and experimental support. Myfab is funded by the Swedish Research Council (2019-00207) as a national research infrastructure. Operation of the Tandem accelerator at Uppsala University is supported through funding from the Swedish Research Council VR-RFI under contract 2019-00191.

Support from the Swedish Foundation for Strategic Research (SSF) for the grant “Development of Processes and Materials in AM (No. GMT14–0048)” and from the Swedish Energy Agency (research project grant P48716-1) are gratefully acknowledged, as well as financial support from the Swedish Research Council (2022-03069).

Appendix A. Supplementary material

Supplementary material related to this article can be found online at <https://doi.org/10.1016/j.matdes.2024.113199>.

References

- [1] S. Pauly, L. Löber, R. Petters, M. Stoica, S. Scudino, U. Kühn, J. Eckert, Processing metallic glasses by selective laser melting, *Mater. Today* 16 (2013) 37–41.
- [2] C. Zhang, D. Ouyang, S. Pauly, L. Liu, 3D printing of bulk metallic glasses, *Mater. Sci. Eng., R Rep.* 145 (2021) 100625, <https://doi.org/10.1016/j.mser.2021.100625>.
- [3] A. Aliyu, A. Azeez, C. Panwisawas, J. Shinjo, C. Puncreobutr, R.C. Reed, K. Pongursiri, B. Lohwongwatana, Laser-based additive manufacturing of bulk metallic glasses: recent advances and future perspectives for biomedical applications, *J. Mater. Res. Technol.* 23 (2023) 2956–2990, <https://doi.org/10.1016/j.jmrt.2023.01.184>.
- [4] H. Liu, D. Yang, Q. Jiang, Y. Jiang, W. Yang, L. Liu, L. Zhang, Additive manufacturing of metallic glasses and high-entropy alloys: significance, unsettled issues, and future directions, *J. Mater. Sci. Technol.* 140 (2023) 79–120, <https://doi.org/10.1016/j.jmst.2022.09.006>.
- [5] M.M. Trexler, N.N. Thadhani, Mechanical properties of bulk metallic glasses, *Prog. Mater. Sci.* 55 (2010) 759–839, <https://doi.org/10.1016/j.pmatsci.2010.04.002>.
- [6] M. Chen, A brief overview of bulk metallic glasses, *NPG Asia Mater.* 3 (2011) 82–90, <https://doi.org/10.1038/asiamat.2011.30>.
- [7] J. Schroers, Bulk metallic glasses, *Phys. Today* 66 (2013) 32–37, <https://doi.org/10.1063/PT.3.1885>.
- [8] L. Jiang, M. Bao, Y. Dong, Y. Yuan, X. Zhou, X. Meng, Processing, production and anticorrosion behavior of metallic glasses: a critical review, *J. Non-Cryst. Solids* 612 (2023) 122355, <https://doi.org/10.1016/j.jnoncrysol.2023.122355>.
- [9] L. Zhang, Z. Jia, F. Lyu, S. Liang, J. Lu, A review of catalytic performance of metallic glasses in wastewater treatment: recent progress and prospects, *Prog. Mater. Sci.* 105 (2019) 100576, <https://doi.org/10.1016/j.pmatsci.2019.100576>.
- [10] A. Inoue, F.L. Kong, Y. Han, S.L. Zhu, A. Churyumov, E. Shalaan, F. Al-Marzouki, Development and application of Fe-based soft magnetic bulk metallic glassy inductors, *J. Alloys Compd.* 731 (2018) 1303–1309.
- [11] G. Herzer, Modern soft magnets: amorphous and nanocrystalline materials, *Acta Mater.* 61 (2013) 718–734.
- [12] Z. Mahbooba, L. Thorsson, M. Unosson, P. Skoglund, H. West, T. Horn, C. Rock, E. Vogli, O. Harrysson, Additive manufacturing of an iron-based bulk metallic glass larger than the critical casting thickness, *Appl. Mater. Today* 11 (2018) 264–269.
- [13] L. Wang, H. Wang, Y. Liu, Z. Fu, T. Peng, J. Shen, S. Zhou, M. Yan, G. Wang, Y. Dai, Selective laser melting helps fabricate record-large bulk metallic glass: experiments, simulation and demonstrative part, *J. Alloys Compd.* 808 (2019) 151731.
- [14] W. Wu, X. Li, Q. Liu, J.Y.F. Hsi, A. Zheng, Y. Zhou, L. Ren, G. Li, Additive manufacturing of bulk metallic glass: principles, materials and prospects, *Mater. Today Adv.* 16 (2022) 100319, <https://doi.org/10.1016/j.mtadv.2022.100319>.

- [15] L. Thorsson, M. Unosson, M.T. Pérez-Prado, X. Jin, P. Tiberto, G. Barrera, B. Adam, N. Neuber, A. Ghavimi, M. Frey, R. Busch, I. Gallino, Selective laser melting of a Fe-Si-Cr-B-C-based complex-shaped amorphous soft-magnetic electric motor rotor with record dimensions, *Mater. Des.* 215 (2022) 110483, <https://doi.org/10.1016/j.matdes.2022.110483>.
- [16] Ł. Żrodowski, R. Wróblewski, M. Leonowicz, B. Morończyk, T. Choma, J. Giftci, W. Świążkowski, A. Dobkowska, E. Ura-Bińczyk, P. Błyskun, et al., How to control the crystallization of metallic glasses during laser powder bed fusion? Towards part-specific 3d printing of in situ composites, *Addit. Manuf.* 76 (2023) 103775.
- [17] J.M. Silveyra, E. Ferrara, D.L. Huber, T.C. Monson, Soft magnetic materials for a sustainable and electrified world, *Science* 362 (2018) eaao0195, <https://doi.org/10.1126/science.aao0195>.
- [18] O. Gutfleisch, M.A. Willard, E. Brück, C.H. Chen, S. Sankar, J.P. Liu, Magnetic materials and devices for the 21st century: stronger, lighter, and more energy efficient, *Adv. Mater.* 23 (2011) 821–842.
- [19] R. Hasegawa, D. Azuma, Impacts of amorphous metal-based transformers on energy efficiency and environment, *J. Magn. Magn. Mater.* 320 (2008) 2451–2456, publisher: North-Holland.
- [20] E.A. Theisen, Recent advances and remaining challenges in manufacturing of amorphous and nanocrystalline alloys, *IEEE Trans. Magn.* 58 (2022) 1–7, <https://doi.org/10.1109/TMAG.2022.3163713>.
- [21] S. Urbanek, B. Ponick, A. Taube, K.P. Hoyer, M. Schaper, S. Lammers, T. Lieneke, D. Zimmer, Additive manufacturing of a soft magnetic rotor active part and shaft for a permanent magnet synchronous machine, in: 2018 IEEE Transportation Electrification Conference and Expo (ITEC), 2018, pp. 668–674.
- [22] A. Plotkowski, J. Pries, F. List, P. Nandwana, B. Stump, K. Carver, R. Dehoff, Influence of scan pattern and geometry on the microstructure and soft-magnetic performance of additively manufactured fe-si, *Addit. Manuf.* 29 (2019) 100781.
- [23] D. Goll, D. Schuller, G. Martinek, T. Kunert, J. Schurr, C. Sinz, T. Schubert, T. Bernthaler, H. Riegel, G. Schneider, Additive manufacturing of soft magnetic materials and components, *Addit. Manuf.* 27 (2019) 428–439.
- [24] E.A. Périgo, J. Jacimovic, F.G. Ferré, L.M. Scherf, Additive manufacturing of magnetic materials, *Addit. Manuf.* 30 (2019) 100870.
- [25] T. DebRoy, H.L. Wei, J.S. Zuback, T. Mukherjee, J.W. Elmer, J.O. Milewski, A.M. Beese, A. Wilson-Heid, A. De, W. Zhang, Additive manufacturing of metallic components – process, structure and properties, *Prog. Mater. Sci.* 92 (2018) 112–224, <https://doi.org/10.1016/j.pmatsci.2017.10.001>.
- [26] X.P. Li, C.W. Kang, H. Huang, T.B. Sercombe, The role of a low-energy-density re-scan in fabricating crack-free Al85Ni5Y6Co2Fe2 bulk metallic glass composites via selective laser melting, *Mater. Des.* 63 (2014) 407–411, <https://doi.org/10.1016/j.matdes.2014.06.022>.
- [27] H.Y. Jung, S.J. Choi, K.G. Prashanth, M. Stoica, S. Scudino, S. Yi, U. Kühn, D.H. Kim, K.B. Kim, J. Eckert, Fabrication of fe-based bulk metallic glass by selective laser melting: a parameter study, *Mater. Des.* 86 (2015) 703–708.
- [28] D.C. Hofmann, P. Bordeenithikasem, A. Pate, S.N. Roberts, E. Vogli, Developing processing parameters and characterizing microstructure and properties of an additively manufactured fccm0bc metallic glass forming alloy, *Adv. Eng. Mater.* 20 (2018) 1800433.
- [29] Y.M. Zou, Y.S. Wu, K.F. Li, C.L. Tan, Z.G. Qiu, D.C. Zeng, Selective laser melting of crack-free Fe-based bulk metallic glass via chessboard scanning strategy, *Mater. Lett.* 272 (2020) 127824, <https://doi.org/10.1016/j.matlet.2020.127824>.
- [30] J.J. Marattukalam, V. Pacheco, D. Karlsson, L. Riekehr, J. Lindwall, F. Forsberg, U. Jansson, M. Sahlberg, B. Hjörvarsson, Development of process parameters for selective laser melting of a zr-based bulk metallic glass, *Addit. Manuf.* 33 (2020) 101124.
- [31] Ł. Żrodowski, B. Wysocki, R. Wróblewski, A. Krawczyńska, B. Adamczyk-Cieślak, J. Zdunek, P. Błyskun, J. Ferenc, M. Leonowicz, W. Świążkowski, New approach to amorphization of alloys with low glass forming ability via selective laser melting, *J. Alloys Compd.* 771 (2019) 769–776.
- [32] D. Ouyang, W. Xing, N. Li, Y. Li, L. Liu, Structural evolutions in 3d-printed fe-based metallic glass fabricated by selective laser melting, *Addit. Manuf.* 23 (2018) 246–252.
- [33] D. Ouyang, P. Zhang, C. Zhang, L. Liu, Understanding of crystallization behaviors in laser 3d printing of bulk metallic glasses, *Appl. Mater. Today* 23 (2021) 100988.
- [34] C. Li, Z.Y. Liu, X.Y. Fang, Y.B. Guo, Residual stress in metal additive manufacturing, *Proc. CIRP* 71 (2018) 348–353, <https://doi.org/10.1016/j.procir.2018.05.039>.
- [35] L. Parry, I.A. Ashcroft, R.D. Wildman, Understanding the effect of laser scan strategy on residual stress in selective laser melting through thermo-mechanical simulation, *Addit. Manuf.* 12 (2016) 1–15.
- [36] H. Liu, Y. Jiang, D. Yang, Q. Jiang, W. Yang, Pores and cracks in the metallic glasses prepared by laser powder bed fusion, *J. Mater. Res. Technol.* 26 (2023) 3070–3089, <https://doi.org/10.1016/j.jmrt.2023.08.061>.
- [37] J.M.D. Coey, *Magnetism and Magnetic Materials*, Cambridge University Press, 2010.
- [38] B.D. Cullity, C.D. Graham, *Introduction to Magnetic Materials*, John Wiley & Sons, 2011.
- [39] R. Schäfer, Domains in ‘extremely’ soft magnetic materials, *J. Magn. Magn. Mater.* 215 (2000) 652–663.
- [40] Y. Zhu, *Modern Techniques for Characterizing Magnetic Materials*, Springer, 2005.
- [41] Eos m100 data sheet, https://www.eos.info/03_system-related-assets/system-related-contents/_pdf_system-data-sheets/eos_system_data_sheet_eos_m_100_en.pdf. (Accessed 9 January 2023).
- [42] G. Nagy, H.J. Whitlow, D. Primetzhofer, The scanning light ion microprobe in Uppsala–status in 2022, *Nucl. Instrum. Methods Phys. Res., Sect. B, Beam Interact. Mater. Atoms* 533 (2022) 66–69.
- [43] P. Ström, D. Primetzhofer, Ion beam tools for nondestructive in-situ and in-operando composition analysis and modification of materials at the tandem laboratory in Uppsala, *J. Instrum.* 17 (2022) P04011.
- [44] J.A. Leavitt, L.C. McIntyre Jr, M.D. Ashbaugh, J.G. Oder, Z. Lin, B. Dezfouly-Arjomandy, Cross sections for 170.5 backscattering of 4He from oxygen for 4He energies between 1.8 and 5.0 mev, *Nucl. Instrum. Methods Phys. Res., Sect. B, Beam Interact. Mater. Atoms* 44 (1990) 260–265.
- [45] A. Guittoum, A. Layadi, H. Tafat, N. Souami, Structural, microstructural and hyperfine properties of nanocrystalline iron particles, *J. Magn. Magn. Mater.* 322 (2010) 566–571.
- [46] Z.J. Zhang, B.X. Liu, Correlation of electron/atom ratio with structural stability in mo-fe, mo-co, and mo-ni alloys, *J. Phys. Condens. Matter* 7 (1995) L293.
- [47] S. Rundqvist, et al., X-ray investigations of the ternary system fe-pb. Some features of the systems cr-pb, mn-pb, co-pb and ni-pb, *Acta Chem. Scand.* 16 (1962) 1–19.
- [48] H. Krainer, Röntgenographische untersuchung der karbide in wolfram-, molybdän- und vanadinstählen, *Arch. Eisenhüttenwes.* 21 (1950) 39–41.
- [49] P. Mercelis, J.P. Kruth, Residual stresses in selective laser sintering and selective laser melting, *Rapid Prototyping J.* 12 (2006) 254–265.
- [50] A. Hussein, L. Hao, C. Yan, R. Everson, Finite element simulation of the temperature and stress fields in single layers built without-support in selective laser melting, *Mater. Des.* 52 (2013) 638–647.
- [51] G. Vastola, G. Zhang, Q.X. Pei, Y.W. Zhang, Controlling of residual stress in additive manufacturing of ti6al4v by finite element modeling, *Addit. Manuf.* 12 (2016) 231–239.
- [52] R. Sharma, A. Kumar, Track-scale simulations of selective laser melting to investigate development and mitigation of thermal stresses, *Lasers Manuf. Mater. Process.* 6 (2019) 464–492.
- [53] J.F. Li, I.V. Soldatov, X.C. Tang, B.Y. Sun, R. Schäfer, S.L. Liu, Y.Q. Yan, H.B. Ke, Y.H. Sun, J. Orava, et al., Metallic mimosa pudica: a 3d biomimetic buckling structure made of metallic glasses, *Sci. Adv.* 8 (2022) eabm7658.
- [54] U.S. Bertoli, G. Guss, S. Wu, M.J. Matthews, J.M. Schoenung, In-situ characterization of laser-powder interaction and cooling rates through high-speed imaging of powder bed fusion additive manufacturing, *Mater. Des.* 135 (2017) 385–396.
- [55] R. Cunningham, C. Zhao, N. Parab, C. Kantzos, J. Pauza, K. Fezzaa, T. Sun, A.D. Rollett, Keyhole threshold and morphology in laser melting revealed by ultrahigh-speed X-ray imaging, *Science* 363 (2019) 849–852.